SATELLITE BASED SHORT-TERM FORECASTING OF SOLAR IRRADANCE - COMPARISON OF METHODS AND ERROR ANALYSIS -

Annette Hammer, Detlev Heinemann, Carsten Hoyer, Elke Lorenz

Department of Energy and Semiconductor Research, Faculty of Physics
Carl von Ossietzky Universität, D-26111 Oldenburg

Abstract

Forecasting of solar irradiance will become a major issue in the future integration of solar energy resources into existing energy supply structures. As far as short-term time horizons (up to 2h) are concerned, satellite data are a high quality source for information about radiation with excellent temporal and spatial resolution. Due to the strong impact of cloudiness on surface irradiance the description of the temporal development of the cloud situation is essential for irradiance forecasting. As a measure of cloudiness, cloud index images according to the Heliosat method are calculated from METEOSAT images. To predict the future cloud index image from a sequence of subsequent images different approaches were applied. A statistical method was used to derive motion vector fields from two consecutive images. The future image then is determined by applying the calculated motion vector field to the actual image. As a completely different approach Neural Networks in combination with Principal Component Analysis were used to describe the development of the cloud structure. The accuracy of the predicted cloud images was analysed and compared for both methods. Motion vector fields showed a superior performance and were chosen for further evaluations. Finally, solar surface irradiance was derived from the predicted cloud index images with the Heliosat method and compared to ground measurements.

1 Introduction

A major challenge of the next decade in global development will be the large scale introduction of renewable energy sources into existing energy supply structures. This not only demands substantial efforts in further developments of advanced technologies but also makes the availability of precise information on the fluctuating resources wind and solar an indispensible necessity. Any efficient use of wind and solar energy conversion processes has to account for this behaviour in respective operating strategies. A key issue hereby is the prediction of renewable energy fluxes, typically for time scales from sub-hour range up to two days depending on the given application. Examples are the storage management in stand-alone photovoltaic or wind energy systems, control of solar thermal power plants and the management of electricity grids with high penetration rates from renewable sources. In this context, this paper focusses on forecasting the surface solar irradiance in a short-term time range of 30 minutes to 2 hours.

The most important atmospheric parameter influencing solar irradiance is cloudiness. Thus forecasting of solar irradiance requires the description of the development of the cloud situation. Information on the spatial stucture of clouds is needed in addition to information on the temporal change of cloudiness. METEOSAT data with their high temporal and spatial resolution can provide this information.

Figure1 gives an overview of the papers main elements. The next chapter briefly describes the calculation of cloud index images from satellite images and the derivation of ground irradiance from the cloud index images using the Heliosat method.

In the third chapter two methods for forecasting cloud images are presented. As the development of the cloud situation is strongly determined by the movement of clouds, the first approach focuses on this issue. A statistically

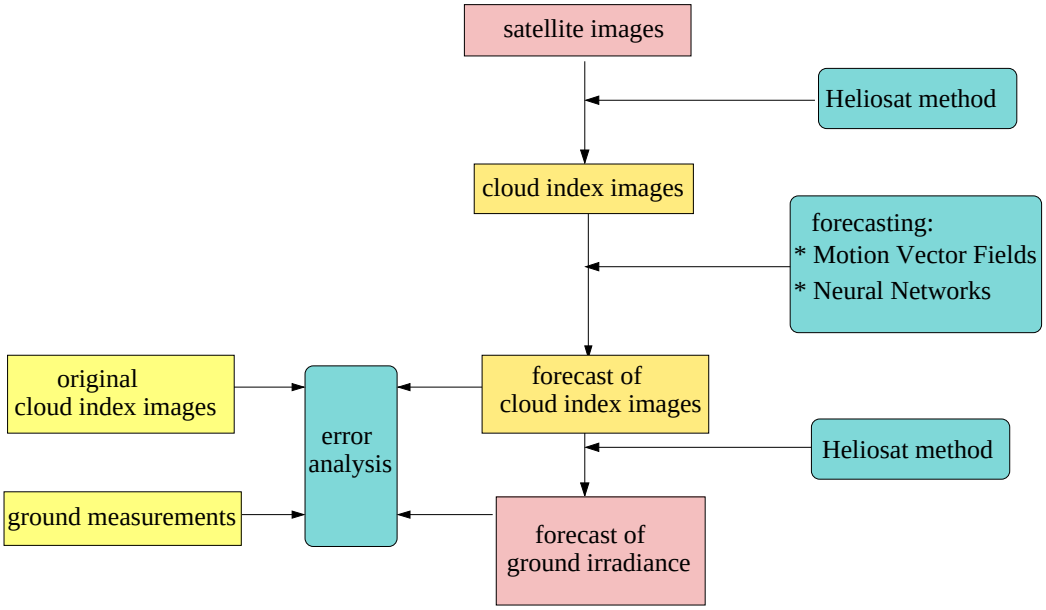

Figure 1: Schematic diagram of the forecast routine and error analysis.

based algorithm for the estimation of motion is applied on two consecutive images to calculate a vector field, that is assumed to describe the motion from one image to the next. This motion vector field (MVF) is applied to the latest image to derive the forecast image. In a second approach additional influences on cloud development like formation and dissolution of clouds are taken into account. Informations of two cloud index images are used as input for a Neural Network (NN), that produces the forecast image as output. The images are classified and principal components are calculated before the NN is applied. Comparison of the two methods showed that the method using MVF performed superior to the NN approach. Therefore the forecast with MVF was used for further claculations of ground irradiance.
Finally the overall performance of the method was tested. The satellite based forecast of ground irradiance was compared to groud measurements for a single station and an ensemble of spatially distributed stations.

2 Calculation of cloud and radiation maps

The forecasting schemes presented in this study use data from the visible sprectral range of METEOSAT. The calculation of cloud index images from original satellite data and of the final irradiance products (see Fig. 1) is done using the operational Heliosat technique described in [1] and [3]. A characteristic feature of the method is the derivation of a dimensionless cloud index value n describing the influence of cloudiness on atmospheric transmittance. Further a quasi linear relationship is assumed between the cloud index n and the ratio of global irradiance G and clear-sky irradiance G_{clear}, referred to as the clear-sky index $k^{\star}$. Typical deviations of the satellite-derived surface irradiance from ground truth data are 20-25 % of relative r.m.s.e. for hourly data. Daily and monthly values generally show uncertainties of 8-12 % and 5-7 %, respectively.
According to the strong influence of clouds on surface solar irradiance forecasts of the cloud index n can be used to determine the future irradiance. The advantage of operating on cloud index images instead of irradiance maps is the independency from daily irradiance pattern.

3 Forecasting Cloud Images

3.1 Motion Vector Fields and Neural Networks

Two different approaches were used to forecast cloud index images, they are illustrated in Fig. 2.
The first approach, the calculation of Motion Vector Fields (MVF), is based on the assumption that the change of the spatial cloud structure is mainly caused by cloud motion. As only larger structures are preserved from one image to the next and small structures vary randomly on short time scales, a smoothing filter is applied to the images before

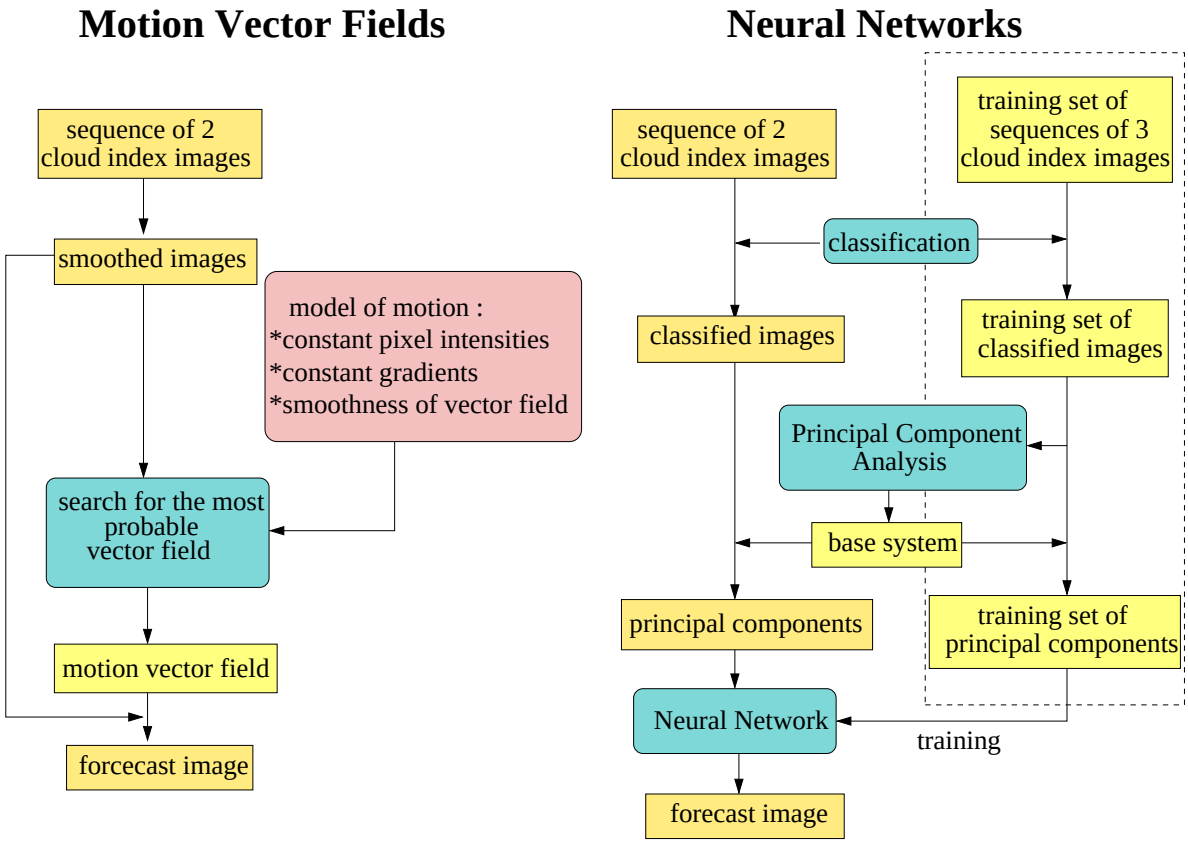

Figure 2: Schematic diagram of the two forecast methods compared within this study.

the Motion Vector Fields are determined.
To find the displacement field that describes best the motion related to two consecutive images, a statistical approach based on a model developed by Konrad and Dubois [4] was applied [2]. In a model of motion the following assumptions for a probable vector field are made, where the displacemnet field is denoted as d, the images as g_0 and g_1 and the position in the image as x_i:

- Pixel intensities are almost constant during motion,

$$U_1 = \sum_i [g_1(x_i + d(x_i)) - g_0(x_i)] \quad \text{is small.} \tag{1}$$

- Gradients of pixel intensities are almost constant,

$$U_2 = \sum_i [\nabla g_1(x_i + d(x_i)) - \nabla g_0(x_i)] \quad \text{is small.} \tag{2}$$

- The displacement field is smooth, neighbouring vectors ($i, j \in \mathbb{N}$) do not differ much from each other,

$$U_3 = \sum_{i,j \in \mathbb{N}} |d(x_i) - d(x_j)|^2 \quad \text{is small.} \tag{3}$$

The probability $P(d|g_0, g_1)$ of a vector field then can be described as:

$$P(d|g_0, g_1) = \frac{1}{Z} e^{-U} \tag{4}$$

with $U = U_1 + U_2 + U_3$ and Z a normalization constant. The most probable vector field is found by minimizing the energy function U. This is done with the statistical method of simulated annealing [2][4].
For the prediction of a cloud index image the calculated MVF is applied to the current image using the assumption that motion changes only slowly with time. Depending on the forecast horizon, the images are smoothed again with

a smoothing mask size increasing with the forecast horizon.
As a second completely different approach Neural Networks (NN) were used to predict the cloud index images. Input for the Neural Network are transformations of two consecutive images, the forecast image is given as output of the NN. Here no assumptions about the dynamics of the cloud structures are made. The development of the cloud situation is learned from a set of sequences of cloud index images, the training set.
As shown in Fig. 2 several steps have to be performed in order to apply the NN to the images. In a first step the examples are divided in four classes depending on mean value and variability of the image pixel intensities. This significantly reduces the error of the Principle Component transformation, which is performed as a next step. Application of the Principle Component Analysis results in the derivation of an optimum base system in a sense that images can be described by only a few modes (components) with the smallest error possible. The first modes represent large scale structures, whereas the higher modes represent the randomly varying small scale structures. Thus using just the principle components, most of the noise is filtered out. An important benefit in using the Principle Component transformation is the significant reduction of input and output dimensions of the NN. Instead of the pixel values the principle components of two consecutive images are used as input for the NN, the output gives the principle components of the image to be forecasted.
With NN the functional dependency between output y and input x is described. This relationship is not known analytically but is learned from a training set. The NN consists of layers of single units, the neurons. For the here used feed forward networks neurons of consecutive layers are connected with weights $w_{i,j}$, thus the activation a for neuron i is given as:

$$a_i = \sum_j w_{i,j} o_j, \tag{5}$$

were o_j is the output of neurons of the previous layer. The input is processed with a sigmoid output function f_{out}, so that the output of the neuron is given as:

$$o_j = f_{out}(a) = f_{out}(\sum_j w_{i,j} o_j). \tag{6}$$

To learn the functional dependency between input and output, the weights $w_{i,j}$ are adjusted such that the difference between net output $N(x)$ and y, the error

$$error = \sum_{(x,y)\in\mathcal{S}} \sum_i (N_i(x) - y_i) \tag{7}$$

is minimized for a training set $\mathcal{S}$. This is achieved using a standard back propagation algorithm. The trained network now can be used to calculate y (forecast image) if x (past and present images) is given.
To find the optimum net configuration, several parameters have to be adjusted, like the number of input neurons ($\sim$ number of modes) and the number of layers and connections. These parameters depend on the image class and the forecast horizon. With increasing forecast horizon the number of predictable modes decreases ($\sim$ 100 modes for 30 min, $\sim$ 10 modes for 120 min). For horizons between 30 and 90 minutes a model with connections of only the same modes from input to output performed best, for a 2 hours horizon the fully connected model gave best results. Hidden layers could improve the forecast quality only in some cases. For the evaluation in chapter 3.2 the results for the respective optimum configurations were taken into account.

3.2 Comparison of both methods

The forecast was evaluated for a 50 day period (14.5.1997 - 2.7.1997) for an area of 250km x 300km situated in North Germany.
As a measure of forecast quality the mean rms errors of pixel values between original images and the forecast were calculated for the time series. This error is presented for both forecast methods and for a persistence forecast as a function of the forecast horizon in Fig. 3. For the numeric calculation the range of cloud index values ([0,..,1]) is mapped into one byte integer values (i.e. [0,..,255]). The results in Fig. 3 are based on this mapping. Both methods reduce the error of persistence, the forecast method using MVF performs significantly better than NN. The MVF method benefits from the additional assumptions that are made about the development of the cloud situation in the model of motion. An attempt to combine the methods and include information about motion in the NN model improved the NN results, but did not outperform the MVF method. Thus the MVF method was chosen for any further evaluations.

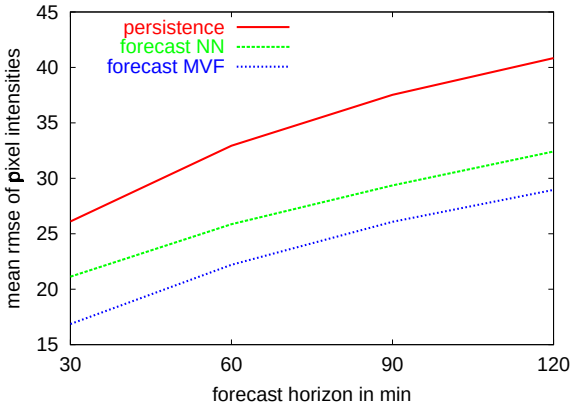

Figure 3: Mean rmse of forcasted image for a time series of 50 days as a function of forecast horizon. The curves correspond to Motion Vector Field forecasts, Neural Net forecasts and persistance (from bottom to top).

4 Evaluation with Ground Data

4.1 Ground Data Set

To evaluate the performance of the radiation forecast, the forecast results were compared to ground measured irradiance. Data from a regional network for measuring global radiation in the region of Saarbrücken (Germany) were used for the month of june 1995. 15 Stations are distributed over an area of 31km x 45km. 7 of these stations are situated on a near distance grid (<7.5km).

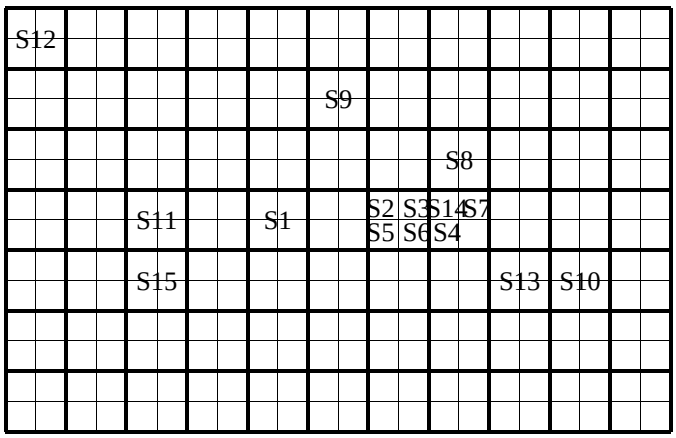

Figure 4: Position of ground stations S1 to S15 in Saarbrücken area in relation to Meteosat images. The large squares represent four Meteosat pixels and an area of approximately 5×7 km^2.

Several configurations were investigated using this setup. The forecast quality was determined for a single station S2 located at 49.24^0N and 6.97^0E, for an ensemble of 8 stations close to this station (ensemble 1) and for an ensemble of 8 stations distributed over the whole area (ensemble 2), see Fig.4. With respect to solar energy applications this correspondes to stand alone systems and grid connected PV systems for local and regional grids, respectivly.

4.2 Results

The forecasted cloud index images were used to calculate half hourly mean values of ground irradiance with the Heliosat method:

$$G_{forec}(x,t) = k^{\star}_{forec}(x,t) G_{clear}(x,t). \tag{8}$$

The overall error of forecasting global radiation includes the error of forecasting the cloud index images and the error of the Heliosat method.

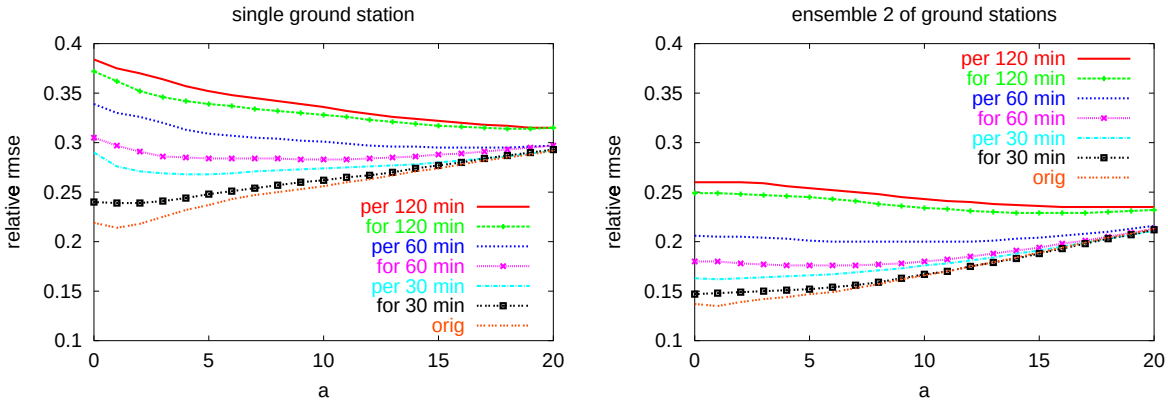

Figure 5: Relative rmse as a function of the number of pixels for different forecast horizons. The results are shown for a single station (left) and ensemble 2 (right).

The match between satellite derived irradiance and ground measurements can be improved by calculating the ground irradiance not only from the pixel corresponding to the ground station, but as a mean of n = $(2a+1)$ x $(2a+1)$ pixels around this station:

$$G_{forec}(x,t) = \sum_{i=0}^{n} k^{\star}_{forec}(x_i,t) G_{clear}(x_i,t) \tag{9}$$

Fig. 5 shows the dependency of the rms error of the time series on the parameter a for a single station and for ensemble 2. The rms error is plotted for G calculated from the original image and from forecast and persistence of cloud index images for different forecast horizons T. G_{per} is calculated as:

$$G_{per}(x,t) = \sum_{i=0}^{n} k^{\star}(x_i, t-T) G_{clear}(x,t). \tag{10}$$

Two effects mainly influence the dependency of the rms error on the number of pixels: As stated in section 3.2 for larger forecast horizons only shapes of large scale structures are predicted due to random variations of small scale structures. Furthermore the error of statistically varying values can be reduced by averaging. The optimum area size for averaging increases with the size of the error. Thus a_{opt} is increasing with the forecast horizon. The difference between forecast and persistence is decreasing with increasing a and for areas of approximately 40 x 40 pixels both, forecast and persistence represent the same pattern and therefore give the same results. A comparison of the figures for a single ground station and ensemble 2 shows that the satellite-based forecast performs better for mean values of an ensemble of stations than for a single station.

This is also illustrated in Fig. 6, where forecasted and measured irradiances as well as the corresponding forecast errors are presented for 5 cloudy days and 5 clear days, respectively. For the cloudy days with larger forecast errors the curves of forecasted and measured irradiance for the ensemble of stations are smoother and match much better than for a single station. For clear days the forecast error is generally small for both, single stations and ensembles of stations.

Fig. 7 shows the forecast errors as a function of the spatial variability in the images, defined as mean difference of intensities g between neighbouring pixels:

$$var = \frac{1}{N} \sum_{i,j \in \mathbb{N}} |g(x_i) - g(x_j)|. \tag{11}$$

From the graph the expected maximum error depending on the variability can be estimated. With increasing spatial variability, which, due to the movement of clouds, is correlated to the temporal variability, forecast results become less reliable.

Finally in Fig. 7 rms errors for the optimum averaging area are shown as a function of the forecast horizon T for a single station, ensemble 1 and ensemble 2. For comparison the rmse for the persistence of cloud images according to Equation 10 is displayed, as well as the rmse for persistence of ground measured $k^{\star}_{gr}$:

$$G_{per,gr}(x,t) = k^{\star}_{gr}(x, t-T) G_{clear}(x,t). \tag{12}$$

As a lower limit for the error of satellite-derived forecasts the error of the Heliosat method is presented. The results for a single ground station and for ensemble 1 are similar, all methods perform only slightly better for ensemble 1.

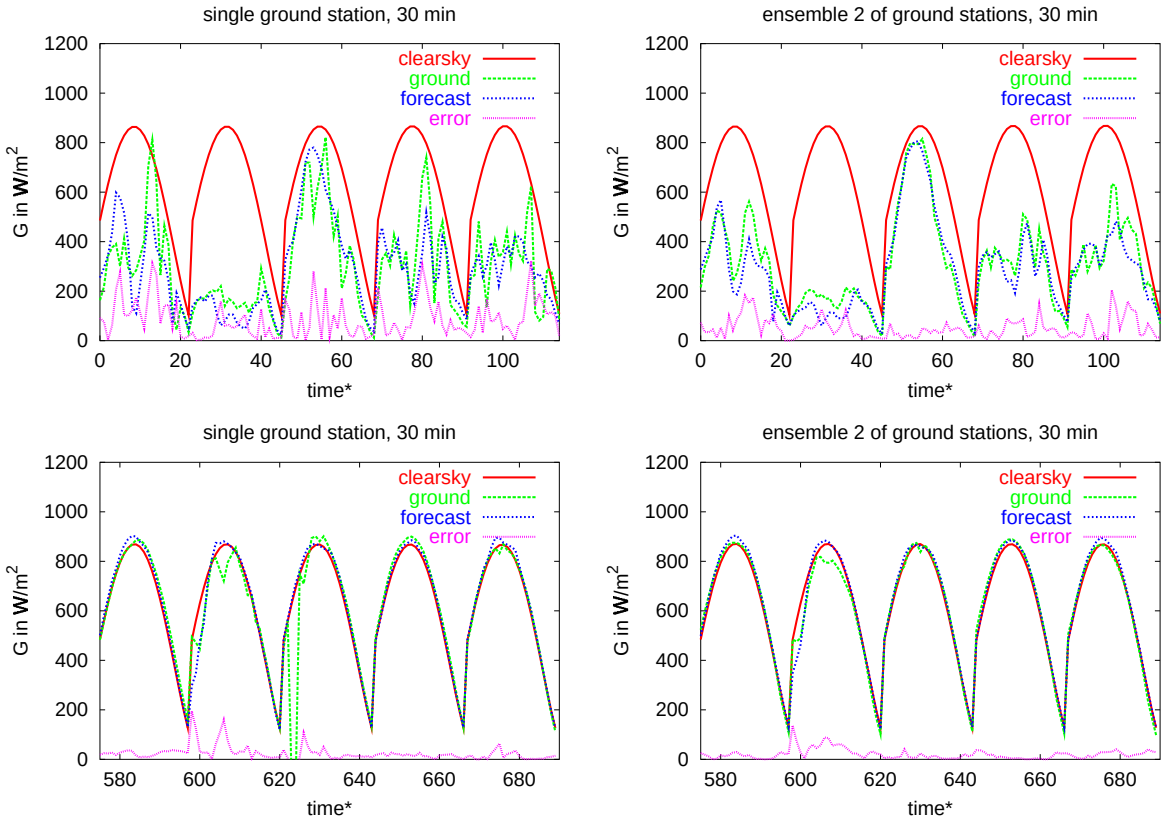

Figure 6: Time series of predicted, ground measured and clearsky irradiance for cloudy days (top) and clear sky days (bottom). In addition, the deviation between predicted and ground measured irradiance is shown.

This is due to the small distances between the ground stations yielding only a small gain in information by adding these stations. For forecast horizons up to 90 minutes the satellite-based forecasts are superior to satellite-based persistence and for a 30 minute horizon the forecast error is slightly higher than the error of the Heliosat method alone. Satellite-based forecast and persistence both outerperform persistence based on ground data due to the spatial information provided by satellite images. The situation is differrent for ensemble 2 with a distribution of the stations over a larger area. Here, for a forecast horizon of 30 minutes persistence based on ground data equals the error of the Heliosat method and is superior to a forecast using only satellite information. For larger forecast horizons the satellite based forecast again gave better results.
Finally, a forecast based on a combination of ground and satellite information

$$G_{gr+sat}(x,t) = \left(\sum_i k^{\star}_{sat}(x_i,t) + c \right) G_{clear}(x,t), \tag{13}$$

was implemented assuming a constant offset

$$c = \sum_{j=0}^{1} \left(\sum_i k^{\star}_{sat}(x_i, t-T-j)) - k^{\star}_{gr}(x, t-T-j) \right) \tag{14}$$

between satellite and ground derived clear sky index $k^{\star}$. The constant c was calculated as an average of the current and the preceeding value. For ensemble 2 and forecast horizons up to 60 minutes this approach showed best results, for a single station and ensemble 1 the satellite-based forecast is most suitable.

5 Conclusion

We have shown that short-term forecasting of cloud index images performs more successful by using Motion Vector Fields than by Neural Networks. This mainly results from the addional information about the cloud motion used in

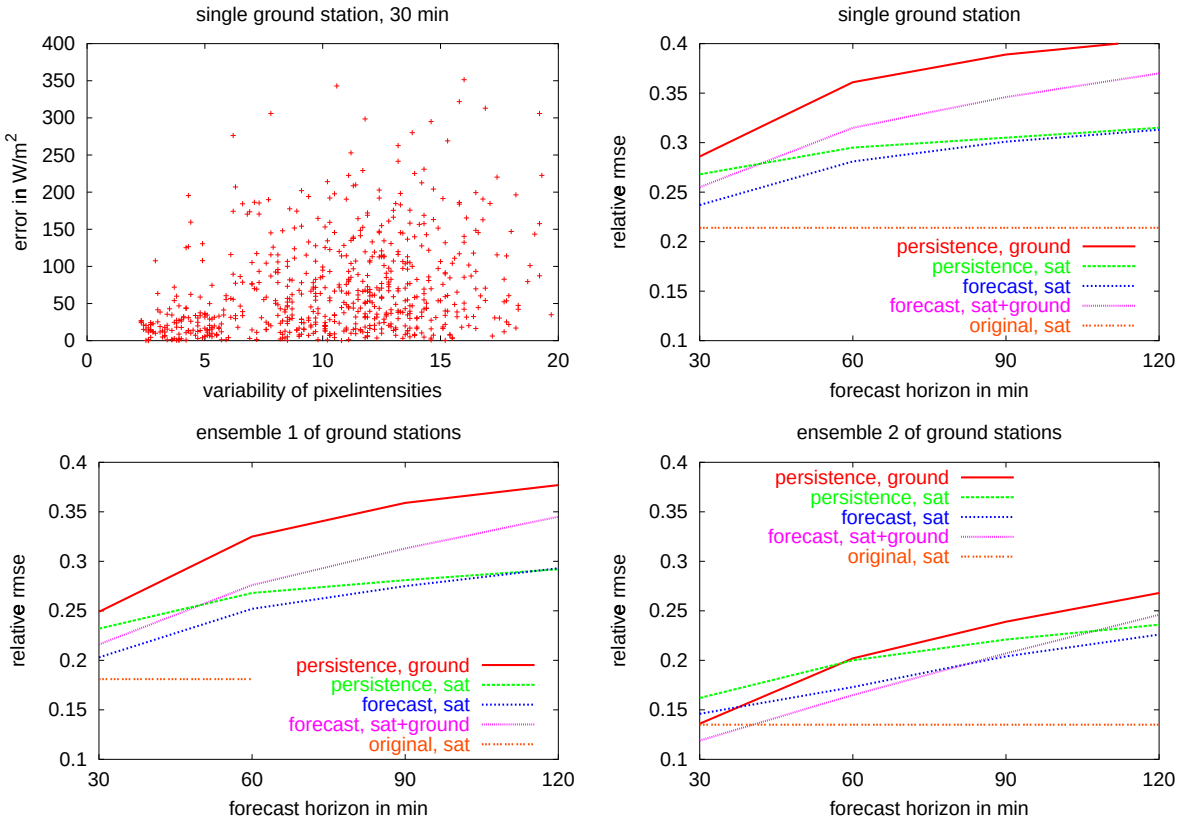

Figure 7: Forecast error as a function of variability of the images (top, left) and rmse as a function of forecast horizon for a single station and the two ensembles of stations.

the MVF method.
Moreover, we investigated the error of forecasted global irradiance for a single ground station and ensembles of spatially distributed stations. For forecast horizons up to 90 minutes global irradiance forecasts show a smaller rms error than the satellite persistence error, which is significantly lowe than the persistence error derived from single station ground data. The error is slightly higher than the error of the Heliosat method applied without forecasting. The average irradiance for an ensemble of stations distributed over several Meteosat pixels can be forecasted with a relative rms of less than 20%. The forecast method is not applicable for forecast horizons larger than 120 minutes.

6 Acknowledgements

We thank G. Luther form the State Institue for Health anf Environment for kindly providing the ground truth data of the Saarbrücken region. We also thank the Universitaetsgesellschaft Oldenburg for supporting parts of this work.

References

[1] Cano D., Monget J.M., Albussion M., Guillard H., Regas N. and Wald L. (1986), *A Method for the Determination of Global Solar Radiation from Meteorological Satellite Data*, Solar Energy 37, 31-39.

[2] Hammer A., Heinemann D., Lorenz E. and Lückehe B., (1999), *Short-Term Forecasting of Solar Radiation based on Image Analysis of Meteosat Data*, Proc. EUMETSAT Meteorological Satellite Data Users Conference, 331-337.

[3] Hammer A., Heinemann D. and Westerhellweg A., (1999), *Daylight and Solar Irradiance Data derived from Satellite Observations - The Satellight Project*, Proc. ISES Solar World Congress, Jerusalem.

[4] Konrad J. and Dubois E. (1992) *Bayesian Estimation of Motion Vector Fields*, IEEE Transactions on Pattern Analysis and Machine Intelligence 11, 910- 927.